Journal of Catalysis 269 (2010) 242–251

Contents lists available at ScienceDirect

Journal of Catalysis

journal homepage: www.elsevier.com/locate/jcat

# Impact of nitrogen doping of carbon nanospheres on the nickel-catalyzed hydrogenation of butyronitrile

Antonio Nieto-Márquez, Diana Toledano, Paula Sánchez, Amaya Romero, José Luis Valverde *

*Facultad de Ciencias Químicas, Departamento de Ingeniería Química, Universidad de Castilla-La Mancha, Campus Universitario s/n, 13071 Ciudad Real, Spain*

ARTICLE INFO

*Article history:*
Received 27 July 2009
Revised 10 November 2009
Accepted 12 November 2009
Available online 16 December 2009

*Keywords:*
Nickel
Carbon nanospheres
Nitrogen doping
Butyronitrile hydrogenation
Nitrogen functionalities

ABSTRACT

Three nickel catalysts supported on carbon and nitrogen-doped carbon nanospheres have been prepared by deposition-precipitation (DP) with urea (ca. 2% w/w). The nanospheres were prepared by thermal pyrolysis of benzene ($CNS_B$), aniline ($CNS_A$) and nitrobenzene ($CNS_N$) and characterized by transmission electron microscopy (TEM), $N_2$ adsorption–desorption, temperature-programmed oxidation (TPO), X-ray diffraction (XRD), elemental (CHN) analysis, X-ray photoelectron spectroscopy (XPS), temperature-programmed decomposition (TPD) and acid/base titrations, revealing different graphitic characteristics and different distribution of nitrogen (when present) functionalities. Upon Ni introduction, the catalysts were characterized by temperature-programmed reduction (TPR), XRD and TEM. Surface area weighted mean Ni particle diameters (post activation at 603 K) were in the range 10.5–18.2 nm. Ni particle size exhibited a big dependence on CNS nitrogen doping, where nitrogen introduction, essentially in the quaternary form, enhanced metal sintering by enriching the surface electron density of the support. The catalysts were tested in the gas phase hydrogenation of butyronitrile ($T$ = 493 K). Extracted specific reaction rates in the steady state followed the sequence: $Ni/CNS_B < Ni/CNS_A < Ni/CNS_N$. When the active metal was physically mixed with the support, the following sequence was obtained: $Ni + CNS_B < Ni + CNS_A < Ni + CNS_N$. Our results demonstrate that doping carbon nanospheres with nitrogen strongly impacts on reactant adsorption and metal sintering, both critical aspects in the hydrogenation of nitriles. Selectivity was not sensitive to the support (or the physical mixture) employed and was in all cases close to 100% to the primary amine.



## 1. Introduction

Carbonaceous materials are widely recognized and employed as catalyst supports, given their unique chemical and physical properties [1]. The growing interest in carbon-related adsorption and catalysis has conducted to a large volume of work devoted to carbon (mainly activated carbon) production [2,3] characterization [4,5], surface modification [6,7] and use [8,9]. Since the discovery of novel carbon nanostructures [10], a lot of research effort has been conducted both in their synthesis and potential applications, given their high mechanical strength, thermal resistance and appreciable surface area [11]. In this sense, filamentous nanostructures, such as carbon nanotubes (CNT) and nanofibers (CNF) have been employed in a number of catalytic reactions, such as hydrogenation [11–13], Fischer-Tropsch [14] and ammonia synthesis [15]. Another novel carbon nanostructure: carbon nanospheres (CNS), has only now started to attract significant research activity. In its spherical arrangement, the graphite sheets are not closed shells but rather waving flakes that follow the curvature of the sphere, creating many open edges at the surface [16]. These unclosed graphitic flakes provide reactive "dangling bonds" that are proposed to enhance surface reactions, establishing CNS as good candidates for catalytic applications [16,17]; however, there is still a dearth of studies dealing with their use in catalysis [18,19].

Doping carbonaceous structures with heteroatoms, such as nitrogen or boron, is an effective means of modifying surface and electronic properties [20,21]. Indeed, it has been established that the incorporation of nitrogen in nanotubes results in enhanced conductivity, polarity and basicity, while modifying surface hydrophilicity [22], where nitrogen can be considered an "n-type" dopant with an extra electron for donation when replacing carbon in the graphitic matrix. According to this, nitrogen doping must have important implications in the catalytic behaviour of carbon supports. Reviewing the existing literature that have compared the catalytic behaviour of nitrogen-doped versus non-doped carbon supports, it is worth flagging the recent work of Amadou et al. [23], who reported a remarkable improvement of the catalytic activity in the liquid phase hydrogenation of cinnamaldehyde when Pd was supported on nitrogen-doped CNT. Raymundo-Piñero et al. [24] reported the catalytic oxidation of $SO_2$ over activated carbon fibers, where nitrogen incorporation, mainly in the form

* Corresponding author. Fax: +34 926295256.
*E-mail address:* joseluis.valverde@uclm.es (J.L. Valverde).

0021-9517/$ - see front matter © 2009 Elsevier Inc. All rights reserved.
doi:10.1016/j.jcat.2009.11.014

of pyridinic groups, increased the catalytic activity. Nitrogen inclusion in different carbon structures has also been reported to enhance the catalytic behaviour towards oxygen reduction and methanol oxidation in fuel cells [25]. The studies cited above point to either electronic or morphological modifications of the active metal phase or the creation of new surface active sites due to nitrogen incorporation. These results open an exciting research path, where a controlled tuning of nitrogen functionalities may conduct to a catalytic improvement, both in terms of activity and selectivity.

Nickel stands as an established hydrogenation metal, which presents low cost and moderate activity [26], in comparison with the more active palladium or platinum [27,28], that could mask to some extent the role of the support. Accordingly, nickel was selected to assess the role of nitrogen inclusion in the catalytic behaviour of carbon nanospheres. Nickel supported on carbon nanospheres (with and without nitrogen) was tested in the gas phase hydrogenation of butyronitrile (BTN). Hydrogenation of nitriles bears industrial interest in the commercial production of amines, given their wide spectrum of industrial applications, being involved in the manufacture of fungicides, chelating agents, surfactants or fine chemicals [29]. Moreover, this reaction presents a structure-sensitive character [30] and the support has been proposed to play an important role in condensation reactions leading to higher amines [31]. We could not find any published study that deals with nitrogen-doping effects in the reduction of a nitrile feed. In the present work, we explicitly establish, for the first time, a clear relationship between nitrogen doping and catalytic activity in the hydrogenation of nitriles.

## 2. Experimental

### 2.1. Support/catalyst preparation and characterization

The three CNS employed in this study were prepared via the thermal pyrolysis (2 h, 1223 K) of benzene ($CNS_B$), aniline ($CNS_A$) and nitrobenzene ($CNS_N$), as described in detail somewhere else [32]. The three CNS-supported Ni catalysts (≈2% w/w) were prepared by deposition-precipitation (DP) using urea as basification agent. Typically, 10 g of CNS were suspended in 1 $dm^3$ of $Ni(NO_3)_2{\cdot}6H_2O$ solution containing excess urea (ca. 5 $mol_{urea}\ mol_{Ni}^{-1}$) and the pH was adjusted to 2–3 by addition of $HNO_3$. The suspension was then heated to 363 K under constant agitation (250 rpm). This procedure ensured the slow decomposition of urea, which contributes to a more homogeneous metal dispersion [33]. After 18 h, the mixture was cooled to room temperature, filtered and the solid thoroughly washed with deionised water until the wash water approached neutral pH. The Ni metal loading was determined by atomic absorption (AA) spectrophotometry, using a SPECTRA 220FS analyzer. Samples (ca. 0.5 g) were treated in 2 $cm^3$ HCl, 3 $cm^3$ HF and 2 $cm^3$ $H_2O_2$ followed by microwave digestion (523 K). Physical mixtures were prepared by mechanically mixing NiO with the supports to yield 2% w/w Ni. All the catalysts were sieved (ATM fine test sieves) into a batch of 75 μm average diameter.

Surface area/porosity measurements were conducted using a Micromeritics ASAP 2010 sorptometer apparatus with $N_2$ as the sorbate at 77 K. All samples were outgassed prior to analysis at 433 K under vacuum ($5 \times 10^{-3}$ Torr) for 16 h. The total specific surface areas were determined by the multipoint BET method and specific total pore volumes were evaluated from $N_2$ uptake at a relative pressure ($P/P_o$) = 0.99. XRD analyses were conducted with a Philips X'Pert instrument using nickel-filtered Cu Kα radiation; the samples were scanned at a rate of 0.02°$step^{-1}$ over the range $5° \leqslant 2\theta \leqslant 90°$ (scan time = 2 s $step^{-1}$) and the diffractograms were compared with the JCPDS-ICDD references [34]. Elemental composition of the carbon supports was determined using a LECO CHNS-932 unit. The carbon (ca. 2 mg) combustion (at 1223 K) products were analyzed by IR (for C and H content) and TCD (for N content). XPS analyses were performed in a SPEC Phoibos system operating with Al ($K_\alpha$) radiation. Peak areas were determined using Shirley's method and the spectra were fitted with Gaussian curves. Sensitivity factors for peaks C1s and N1s were 1 and 1.8 respectively. Acid/base titrations were performed in a Metrohm 686 titrator with a Dosimat 665 automatic dosager. Sample (25 mg) was immersed in 50 $cm^3$ solution of 0.1 M NaCl, acidified to pH ca. 3 with HCl (0.1 M) with constant stirring under a He atmosphere. A 0.1 M NaOH solution was used as the titrant, added dropwise (1.8 $cm^3\ h^{-1}$). The starting NaCl solution served as a blank. Temperature-programmed experiments were conducted in a commercial Micromeritics AutoChem 2950 HP unit with TCD detection. Samples (ca. 0.1 g) were loaded in a U-shaped tube and ramped from room temperature to 1273 K (5 K $min^{-1}$). Temperature-programmed oxidation (TPO) analyses were done in an oxidizing gas mixture ($O_2$/He, 20% v/v, 60 $cm^3\ min^{-1}$), temperature-programmed reduction (TPR) used a reducing gas mixture of 17.5% v/v $H_2$/Ar (60 $cm^3\ min^{-1}$), and temperature-programmed decomposition (TPD) employed pure helium (60 $cm^3\ min^{-1}$). Transmission electron microscopy (TEM) analysis employed a JEOL JEM-4000EX unit with an accelerating voltage of 400 kV. Samples were prepared by ultrasonic dispersion in acetone with a drop of the resultant suspension evaporated onto a holey carbon-supported grid. TEM analyses served to provide a mean Ni particle size, which is quoted in this paper as surface-area weighted ($\overline{d}_S$) according to:

$$\overline{d}_S = \frac{\sum_i n_i d_i^3}{\sum_i n_i d_i^2} \tag{1}$$

where $n_i$ represents the number of particles of diameter $d_i$; $\sum_i n_i \geqslant 400$.

### 2.2. Catalysis procedure

Reactions were conducted at 493 K under atmospheric pressure in a fix bed quartz reactor (600 mm length, 15 mm i.d.). Catalysts were activated in situ to 603 K under TPR conditions and maintained at that temperature for 1 h prior to reaction. Preliminary experiments ruled out the existence of heat/mass transport limitations and the passage of the reactant in the absence of catalyst or support did not result in any appreciable conversion. The butyronitrile feed was delivered to the reactor via a glass/Teflon air-tight syringe and a Teflon line using a microprocessor-controlled infusion pump (Model 100 Kd Scientific). The molar butyronitrile inlet to molar Ni in the bed ratio was maintained at $6.5 \times 10^3\ mol_{BTN}\ h^{-1}\ mol_{Ni}^{-1}$ for the supported catalysts and at $1.6 \times 10^2\ mol_{BTN}\ h^{-1}\ mol_{Ni}^{-1}$ in the case of the physical mixtures. This was a consequence of weighting limitations, that is, it was not possible to weight an (so low) equivalent bulk metal amount as the contained in the supported catalysts. The reverse approach, that is, increasing the amount of supported catalysts to equal the amount of metal present in the bulk system resulted in heat/mass transfer limitations. A co-current flow of $H_2$ (60 $cm^3\ min^{-1}$) was introduced, keeping GSHV = $1 \times 10^4\ h^{-1}$. Same contact time and isothermal conditions (±1 K) were maintained by diluting the catalyst bed with ground glass (75 μm) and the reaction temperature was continuously monitored by a thermocouple located within the catalyst bed. The product stream was collected in a liquid nitrogen trap and analyzed by capillary GC (Shimadzu, Model GC 17 A) with MS detection (Shimadzu, Model GCMS-QP 5000). The column employed was a Petrocol DH (100 m × 0.25 mm i.d.). Butyronitrile

(BTN) conversion and selectivity to the product *i* were calculated according to:

$$X_{BTN}(\%) = \frac{BTN_{in} - BTN_{out}}{BTN_{in}} \times 100 \quad (2)$$

$$S_i(\%) = \frac{Product_{i,out}}{BTN_{in} - BTN_{out}} \times 100 \quad (3)$$

where $BTN_{in}$, $BTN_{out}$ and $Product_{i,out}$ represent the concentration of reactant or products entering (in) or leaving (out) the reactor. These concentrations were calculated from peak areas taking into account the different sensitivity factors and normalized to mol percent, as well as the reaction stoichiometry.

## 3. Results and discussion

### 3.1. Support/catalyst characterization

Transmission electron microscopy was employed to assess the morphological features of the supports. Low resolution TEM micrographs (Fig. 1a–c) show how CNS are present as a conglomeration of spherical bodies with diameters in the range 300–500 nm. The presence of conglomerates has been attributed in the literature to an accretion of individual spheres given their high surface chemical activity [35]. Representative high-resolution TEM micrograph (Fig. 1d) corresponding to $CNS_B$ illustrates the joint between two spheres, showing a markedly graphitic character, with a layered structure and an interlayer distance ($d_{002}$) of ca. 0.34 nm, characteristic of a graphitic material. Arrows in Fig. 1d indicate the open graphitic flakes on the surface of the spheres. BET surface areas and total pore volumes associated with the three supports are given in Table 1. Low surface area/porosity values compare well with the reported for nanospheres grown from diverse precursors under different growth conditions [17,36,37]. Structural features of the support were further investigated by means of TPO and XRD analyses. TPO analyses corresponding to the three CNS supports, and for model graphite (Sigma–Aldrich) are shown in Fig. 2. Profie (I), associated to $CNS_B$ (i.e. CNS without nitrogen) exhibited a single oxidation peak at $T_{max}$ = 920 K, similar to the corresponding to model graphite (dashed line). Comparable oxidation peaks associated to nanostructured carbon materials have been reported elsewhere [36–38], being CO and $CO_2$ the oxidation products [38]. Profiles (II) and (III) correspond to nitrogen containing CNS, that is, $CNS_A$ and $CNS_N$, respectively. Two oxidation peaks at $T_{max}$ = 866 and 944 K associated to $CNS_A$ and $T_{max}$ = 805 and 934 K associated to $CNS_N$ were observed. Comparable two-stage oxidation profiles have been reported before for nitrogen containing carbon, attributed to the release of CO, $CO_2$ and $NO_x$ [39–41]. These reports have shown that the first peak corresponds to the gasification of the graphitic matrix with subsequent release of carbon oxides, with a minor contribution of nitrogen oxides, the latter being essentially released at higher temperatures, that is, second peak, due to nitrogen retention in the char. TPO is widely employed to establish a sequence of graphitic character between different carbonaceous materials, where the more graphitic the material is, the higher the temperature is needed to gasify the carbon structure [42]. In this line, comparing the oxidation peak associated with $CNS_B$ with the first peaks, that is, CO and $CO_2$ release, associated with $CNS_A$ and $CNS_B$, oxidation temperatures consistently shifted to lower values when nitrogen was incorporated in the carbon matrix, sug-

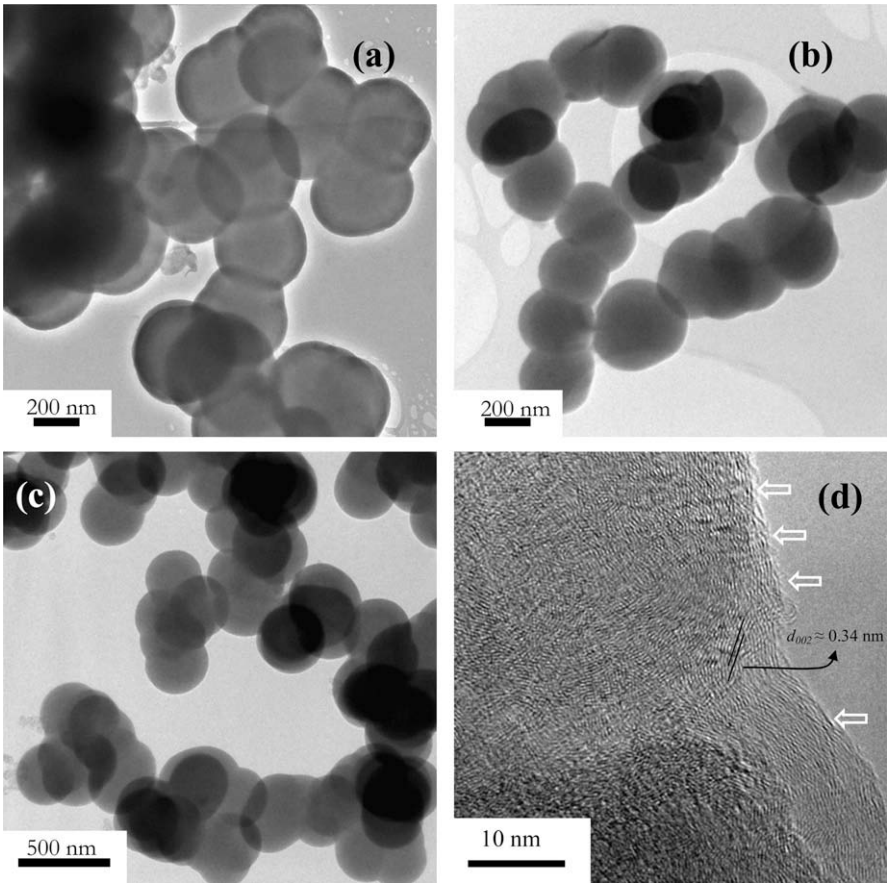


**Fig. 1.** Representative low resolution TEM micrographs of (a) $CNS_B$, (b) $CNS_A$ and (c) $CNS_N$. (d) HRTEM of $CNS_B$.

**Table 1**
Physicochemical properties of the three CNS.

| CNS | BET ($m^2\ g^{-1}$) | Total pore volume ($cm^3\ g^{-1}$) | $d_{002}$ (nm) | $L_C$ (Å) | N/C (at.%) |
|---|---|---|---|---|---|
| $CNS_B$ | 14.3 | 0.05 | 0.336 | 33.0 | 0 |
| $CNS_A$ | 11.8 | 0.03 | 0.336 | 21.9 | 3.5 |
| $CNS_N$ | 9.1 | 0.03 | 0.337 | 18.9 | 2.7 |

gesting a decrease in graphitic character in the sequence $CNS_B > CNS_A > CNS_N$. It is well established that the incorporation of heteroatoms into structured carbon, even at a low mass/mole percent, can induce lattice defects in the graphene layers [43], conducting to a less graphitic material and, thus, easier to oxidize. While TPO analysis provides an indirect assessment of carbon structural order, the inferred trends find further support in XRD. Representative XRD patterns are shown in Fig. 3 and derived crystalline parameters are given in Table 1. Each profile exhibits a main peak at ca. 26°, that is, (0 0 2) graphite plane. We have adopted the interlayer spacing $d_{002}$ and the average crystalline size $L_C$ as quantitative measurements of the graphitic character [44,45]. The $d_{002}$ values recorded in Table 1 are consistent with a graphitic product and $L_C$ increased in the order $CNS_N < CNS_A < CNS_B$, which is in good agreement with the results derived from TPO analyses. Nitrogen to carbon ratio (at.%) is presented in Table 1, being very similar in the two nitrogen-doped spheres (2.7–3.5 at.%). However, XPS analyses shown in Fig. 4, revealed a distinct distribution of nitrogen functionalities. As expected, carbon obtained from benzene did not produce any measurable nitrogen-associated signal, which discards the contribution of physisorbed nitrogen during sample handling/preparation/analysis. After deconvolution of the N1s peak associated with $CNS_A$ and $CNS_N$, at least three different signals were fitted, revealing the presence of different types of nitrogen. Available literature related to nitrogen-doped carbon assigns nitrogen functionalities to pyridinic nitrogen ($N_P$, BE at ca. 398 eV), pyrrolic nitrogen ($N_{PYR}$, BE at ca. 399 eV), quaternary nitrogen ($N_Q$, BE at ca. 401 eV) and adsorbed nitrogen or nitrogen oxides (N–X, BE at ca. 402–405 eV) [23,46,47]. N1s peak associated to carbon obtained from the pyrolysis of aniline (Fig. 4a) exhibited these four contributions, with relative nitrogen amounts of 10.50%, 27.34%, 52.29% and 9.86% corresponding to $N_P$, $N_{PYR}$, $N_Q$ and N–X, respectively. In the case of nitrobenzene as nitrogen–carbon source, the best fitting of the N1s peak (Fig. 4b) conducted to three curves, corresponding to $N_{PYR}$, $N_Q$ and N–X, with relative nitrogen amounts of 7.20%, 77.69% and 15.11%, respectively, with no appreciable contribution from pyridinic nitrogen. This result suggests a more homogeneous distribution of nitrogen species in carbon obtained from the pyrolysis of nitrobenzene. Moreover, different acid/base properties have been attributed in the literature to the different nitrogen functionalities in a carbon matrix. Quaternary nitrogen replaces a carbon atom in the graphitic matrix and the removal of one electron (i.e. uptake of a proton) decreases the aromaticity of the system, what is energetically unfavourable. Thus, no basicity is expected from this type of nitrogen [48]. For pyrrolic nitrogen, the uptake of a proton, as in the case of the quaternary nitrogen, needs the donation of an electron from the aromatic system, with subsequent loss of aromaticity. Again, an acidic rather than basic character is expected from this type of nitrogen [49]. N–X species, mainly as an oxidized form of pyridinic nitrogen, have been found to deliver some acidic behaviour [50]. Pyridinic nitrogen, with a lone electron pair, can behave both as a Lewis and a Brönsted base, being able to uptake protons [48]. Acid/base titrations presented in Fig. 5 show how neither basic nor acidic character was appreciably delivered by the three materials. Only in the case of $CNS_A$, the titration curve ran slightly left from the blank, suggesting some measurable basicity. This is consistent with XPS analyses, where a pyridinic component was revealed for this material. Thus far, we have presented three different nanostructured carbon spheres, where characterization results reveal different graphitic characteristics and distribution of nitrogen (when present) functionalities.

TPR profiles associated with each catalyst are presented in Fig. 6a, where two hydrogen consumptions and a negative peak

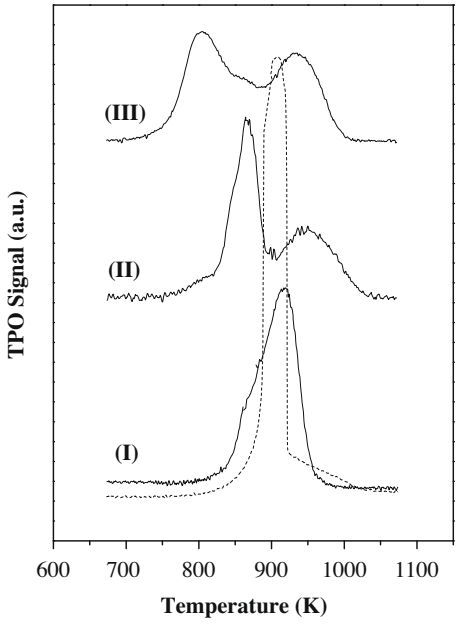


**Fig. 2.** TPO profiles associated with (I) $CNS_B$, (II) $CNS_A$ and (III) $CNS_N$. Dashed line corresponds to model graphite.

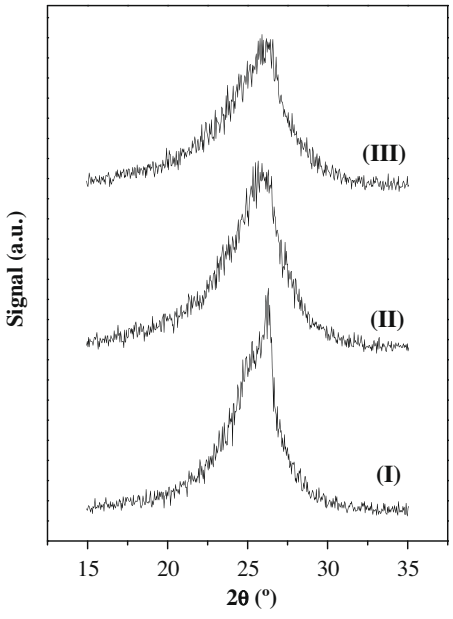


**Fig. 3.** XRD patterns associated with (I) $CNS_B$, (II) $CNS_A$ and (III) $CNS_N$.

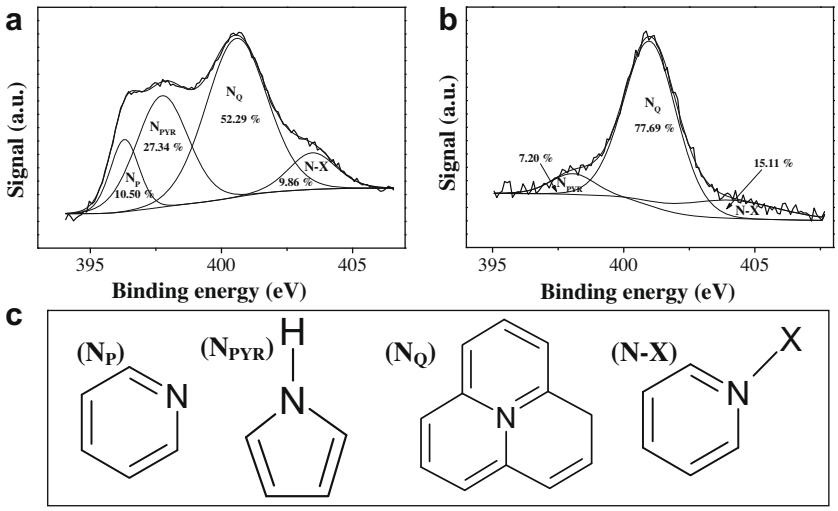


**Fig. 4.** XPS N1s spectra associated with (a) $CNS_A$ and (b) $CNS_N$. (c) Types of nitrogen functionalities.

were present in all cases. The first hydrogen consumption peak, appearing at a $T_{max}$ = 601–610 K is attributed to the reduction of $Ni(OH)_2$ to $Ni^0$. Upon DP synthesis, nickel is attached to the support as $Ni(OH)_2$ [51] and comparable single reduction peaks associated to the reduction of $Ni(OH)_2$ to $Ni^0$ have been reported elsewhere for Ni/C systems prepared in a similar way [19,52]. The second hydrogen consumption resulted in a broader peak with $T_{max}$ in the range 810–850 K, attributable to hydrogen uptake by the support upon decomposition of oxygen surface groups, as reported elsewhere [19,53–55]. Thermal decomposition analyses (in He) of the bare supports are shown in Fig 6b, presenting $T_{max}$ in the range 850–860 K. This TPD response can be ascribed to the release of $CO + CO_2$ resulting from the decomposition of carboxylic anhydride groups [55]. The appearance of a third (negative) peak in the TPR, at temperatures of ca. 1273 K, has been attributed to the hydrogasification of carbon to methane [19,53]. According to what has

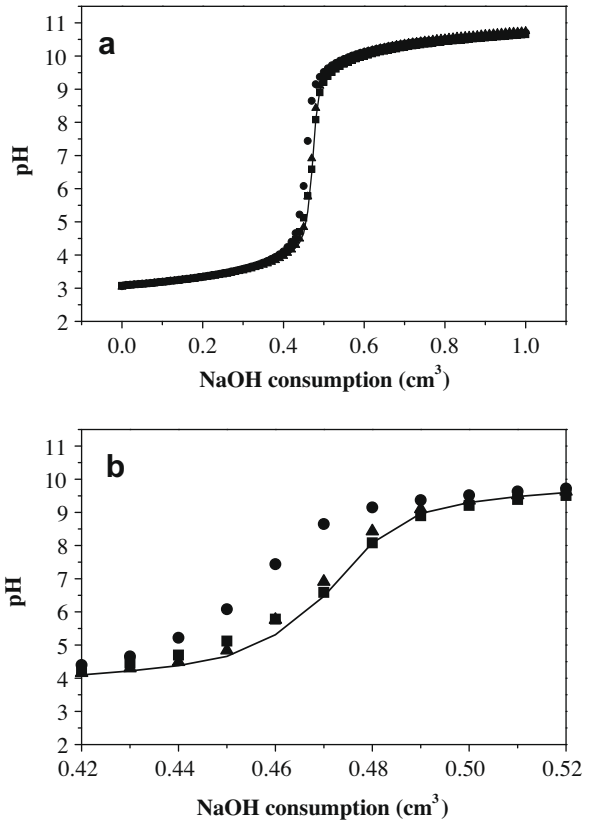


**Fig. 5.** (a) Acid/base titration curves associated with (■) $CNS_B$, (●) $CNS_A$ and (▲) $CNS_N$. Solid line corresponds to the blank. (b) Expanded equivalence point region of titrations.

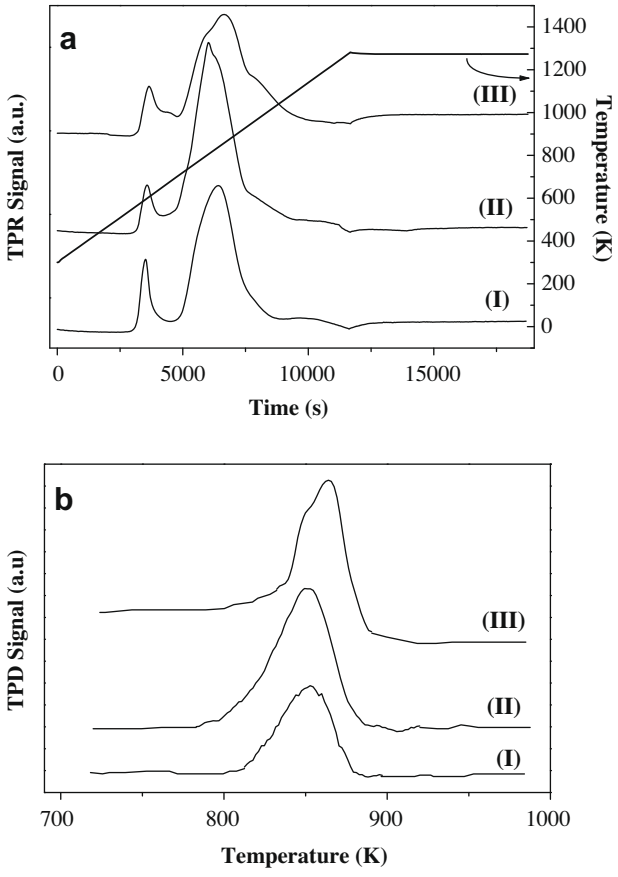


**Fig. 6.** (a) TPR profiles associated with (I) $Ni/CNS_B$, (II) $Ni/CNS_A$ and (III) $Ni/CNS_N$. (b) TPD profiles associated with (I) $CNS_B$, (II) $CNS_A$ and (III) $CNS_N$.

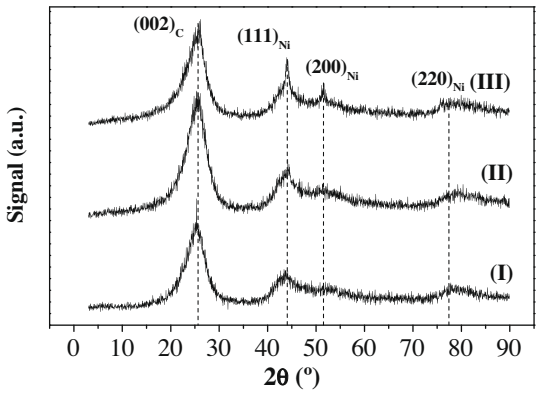


**Fig. 7.** XRD patterns for the activated (I) Ni/$CNS_B$, (II) Ni/$CNS_A$ and (III) Ni/$CNS_N$. Note: dashed lines indicate position for JCPDS-ICDD reference graphite (Card No. 41-1487) and Ni (Card No. 45-1027).

been exposed above, 603 K was chosen as an appropriate temperature to activate nickel. The latter assumption was further investigated by XRD analyses (Fig. 7), where reflections appearing at 44.5°, 51.8° and 76.3° correspond, respectively, to the (1 1 1), (2 0 0) and (2 2 0) planes of metallic nickel and are consistent with an exclusive cubic geometry [34]. The reflection appearing at ca. 26° corresponds to the (0 0 2) graphite plane of carbon; its relationship with carbon crystalline character has been discussed above. Ni particle size and morphology were evaluated by TEM analyses. Representative TEM micrographs of the activated catalysts are presented in Fig. 8. TEM-derived particle size distributions are shown in Fig. 9 and the extracted surface area weighted mean diameters are given in Table 2. Ni/$CNS_B$ exhibited a narrow distribution of well-dispersed nickel particles with $\overline{d}_S$ = 10.5 nm, where relatively thin and faceted particles are diagnostic of a strong interaction with the support [56]. In the case of Ni/$CNS_A$ and Ni/$CNS_N$, a wider distribution of sizes was encountered and $\overline{d}_S$ was shifted to 13.1 and 18.2 nm respectively, where a more dense pseudo-globular morphology suggests a weaker metal-support interaction [56]. The differences in particle sizes and distributions described above must be linked to a different metal mobility during activation, where those particles more weakly attached to the support must sinter in a higher extent. Comparable phenomena have been reported elsewhere for other supported nickel systems [57,58]. Under identical metal introduction method and comparable metal loading (see Table 2), larger nickel particles were those supported on nitrogen-doped spheres, suggesting a modification of the surface energetics of the sphere by nitrogen doping. It is commonly accepted that the introduction of nitrogen atoms into a graphitic matrix lowers the electron work function of the carbon surface. This results in an enhanced electron mobility in comparison with a pure carbon [59,60], this mobility being essentially enhanced when nitrogen is incorporated in a $sp^2$ graphitic arrangement (denoted here as quaternary nitrogen, $N_Q$, Fig. 4), that enriches the density of $\pi$ electrons in the aromatic system [60]. A detailed quantum chemical calculation proposed by Strelko et al. provides further support to what is exposed above [59]. In this line, the sequence of growing particle size: Ni/$CNS_B$ < Ni/$CNS_A$ < Ni/$CNS_N$ is in good agreement with the increase in the presence of quaternary nitrogen (see Fig. 4), that is, a higher electron density must enhance metal motion and subsequent sintering.

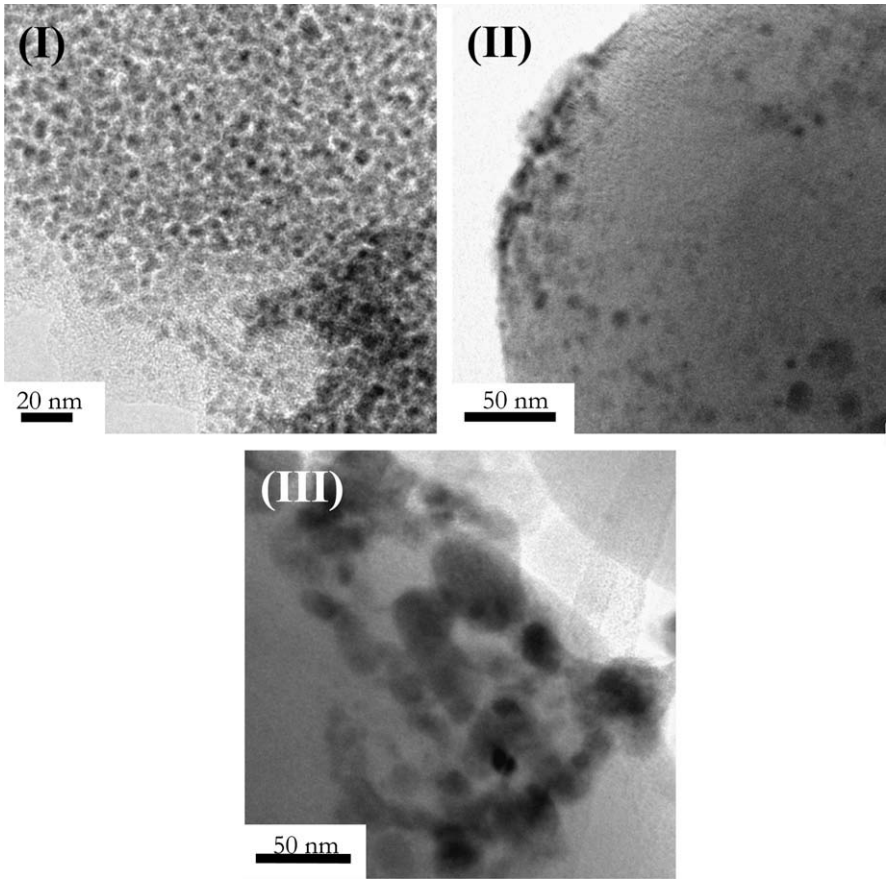


**Fig. 8.** Representative TEM micrographs for the activated (I) Ni/$CNS_B$, (II) Ni/$CNS_A$ and (III) Ni/$CNS_N$.

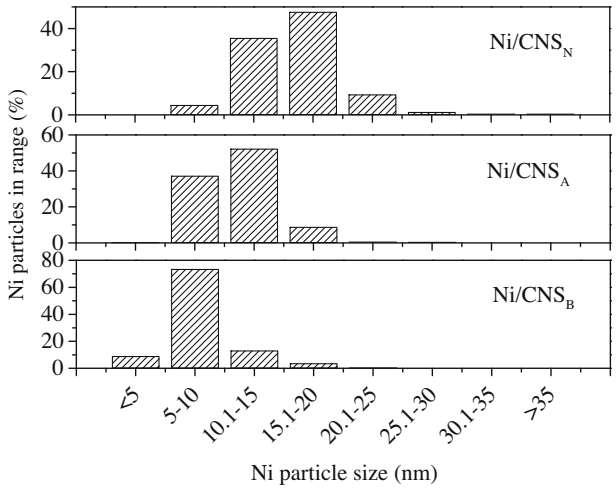


**Fig. 9.** Nickel particle size distributions associated with the activated Ni-supported catalysts.

**Table 2**
Physicochemical properties of the three supported Ni catalysts.

| Catalyst | Ni loading (% w/w) | TPR $T_{max}$ (K)[a] | $\overline{d}_s$ (nm) |
|---|---|---|---|
| Ni/CNS$_B$ | 2.5 | 601 | 10.5 |
| Ni/CNS$_A$ | 1.8 | 603 | 13.1 |
| Ni/CNS$_N$ | 1.8 | 610 | 18.2 |

[a] Values associated with the reduction of the metal precursor, first peak in TPR.

### 3.2. Catalytic activity

The hydrogenation of butyronitrile (BTN) yields its primary amine, mono-*n*-butylamine (MBA) as the main reaction product. It can also lead to the corresponding secondary and tertiary amines; di-*n*-butylamine (DBA) and tri-*n*-butylamine (TBA), respectively. According to von Braun's mechanism for the hydrogenation of nitriles [61], as shown in Fig. 10, MBA is formed via hydrogenation of BTN, passing through the intermediate butylidenimine. Condensation reactions generating secondary and tertiary amines occur via the reactive butylidenimine, which is nucleophilicaly attacked by *n*-butylamine or di-*n*-butylamine. Subsequent elimination of ammonia yields *N*-butylidene-butylamine (BBA) or but-1-enyl-dibutylamine as the condensation products to be finally hydrogenated to DBA or TBA, respectively. In the present work, the hydrogenation of BTN over the tested catalysts yielded MBA as the majority product, as well as minor amounts of DBA and TBA and the intermediate BBA, as will be discussed later. Conversion of BTN (at 493 K) as a function of time-on-stream is presented in Fig. 11. A temporal decline was observed in each case to approach the steady state after ca. 12 hours-on-stream. The deactivation of Ni catalysts during the hydrogenation of nitriles has been studied in detail by Verhaak et al. [62], being acetonitrile the test reactant. They described this deactivation as the result of the two contributions; on the one hand, partially dehydrogenated acetonitrile species can strongly adsorb on the surface of the catalyst covering active sites; on the other hand, decomposition of reactants or products during the process can generate a carbonaceous residue that contaminates the nickel surface. Specific (per metal unit mass, metal unit area and support unit area) reaction rates were extracted in the steady state (see Table 3). Specific Ni surface area ($S_{Ni}$), was calculated according to:

$$S_{Ni} = \frac{6}{\rho_{Ni} \times \overline{d}_s} \quad (4)$$

where 6 is the shape factor assuming a spherical geometry, which can account as a valid assumption based on TEM analysis, $\rho_{Ni}$ is the Ni density (8.9 g cm$^{-3}$) and $\overline{d}_s$ is the surface-weighted mean Ni particle diameter (derived from TEM analyses, see Eq. (1)). The following sequence of increasing activity was obtained: Ni/CNS$_B$ < Ni/CNS$_A$ < Ni/CNS$_N$. Reaction rates obtained in this work compare well with those reported in the literature for the hydrogenation of nitriles over Ni-based catalysts both in the gas [58,63,64] and the liquid [65] phases. It is commonly accepted that larger, that is, less disperse particles develop a higher activity in the hydrogenation of nitriles, as reported by other authors who studied the hydrogenation of acetonitrile in the gas phase over Ni supported on porous-pillared tin phosphates [58] and alumina, titania and sil-

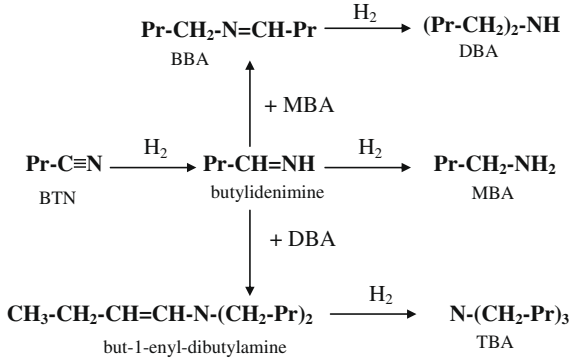


**Fig. 10.** Reaction scheme for BTN hydrogenation.

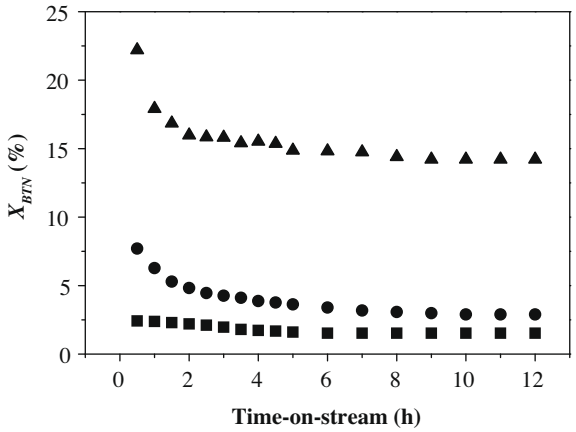


**Fig. 11.** Variation of butyronitrile conversion ($X_{BTN}$) with time-on-stream over (■) Ni/CNS$_B$, (●) Ni/CNS$_A$ and (▲) Ni/CNS$_N$. Inlet: 6.5 × 10$^3$ mol$_{BTN}$ h$^{-1}$ mol$_{Ni}^{-1}$.

**Table 3**
Specific reaction rates associated with supported and unsupported catalysts.

| Catalyst | Rates | | |
|---|---|---|---|
| | mol$_{BTN}$ h$^{-1}$ g$_{Ni}^{-1}$ | 10$^2$ × (mol$_{BTN}$ h$^{-1}$ m$_{Ni}^{-2}$) | 10$^3$ × (mol$_{BTN}$ h$^{-1}$ m$_{support}^{-2}$) |
| Ni/CNS$_B$ | 1.7 | 2.6 | 2.9 |
| Ni/CNS$_A$ | 3.2 | 6.1 | 4.8 |
| Ni/CNS$_N$ | 15.5 | 41 | 30 |
| Ni + CNS$_B$[a] | 0.6 | 20 | 4.7 |
| Ni + CNS$_A$[a] | 0.7 | 21 | 6.0 |
| Ni + CNS$_N$[a] | 1.0 | 33 | 12 |

[a] Specific surface area of unsupported Ni (3 m$^2$ g$^{-1}$) was calculated by $N_2$ adsorption/desorption (Ref. [68]).

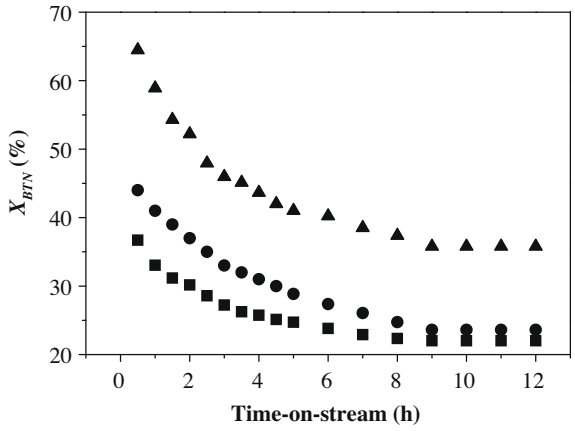


**Fig. 12.** Variation of butyronitrile conversion ($X_{BTN}$) with time-on-stream over (■) Ni + $CNS_B$, (●) Ni + $CNS_A$ and (▲) Ni + $CNS_N$. Inlet: $1.6 \times 10^2$ $mol_{BTN}$ $h^{-1}$ $mol_{Ni}^{-1}$.

ica–alumina [66]. This structure-sensitive behaviour must be linked to metal electronic state; large metal particles (high electron density) weaken the adsorption strength of BTN by repelling the lone electron pair in the nitrogen atom of the cyano group (C≡N). The C≡N bond adsorbs more strongly on smaller particles, becoming more difficult to hydrogenate, as explicitly established by Arai et al. and Li et al. in the case of Pt [30] and Ni [67] catalysts, respectively. This is in good agreement with the activity sequence established above, where bigger particles consistently delivered a higher catalytic activity. So far, we have demonstrated that a proper control in nitrogen doping of carbonaceous materials has an important impact on the electronic properties of the carbon surface and, in turn, on the degree of metal sintering. Therefore, nitrogen doping stands as an effective means of modifying to some extend the metal particle size and subsequently, the related catalytic activity in a structure-sensitive reaction. While the metal particle size plays an important role in this reaction, conclusions cannot be directly drawn without taking into account that reactant configuration may be different on the surface of the different materials. This is a common drawback of supported metal systems, where it is often difficult to decouple different effects that might be acting simultaneously. In the present case, given the established relationship between particle size and catalytic activity, any differential role on reactant adsorption/activation played by the support may keep masked. For this reason, physical mixtures of each support and a nickel precursor (NiO) were tested in the reaction at 493 K, after activation under the same conditions as the supported systems, allowing us to compare the behaviour of the different supports ruling out possible differences in the metallic phase. Upon activation, bulk Ni was presented as a conglomeration of large particles in

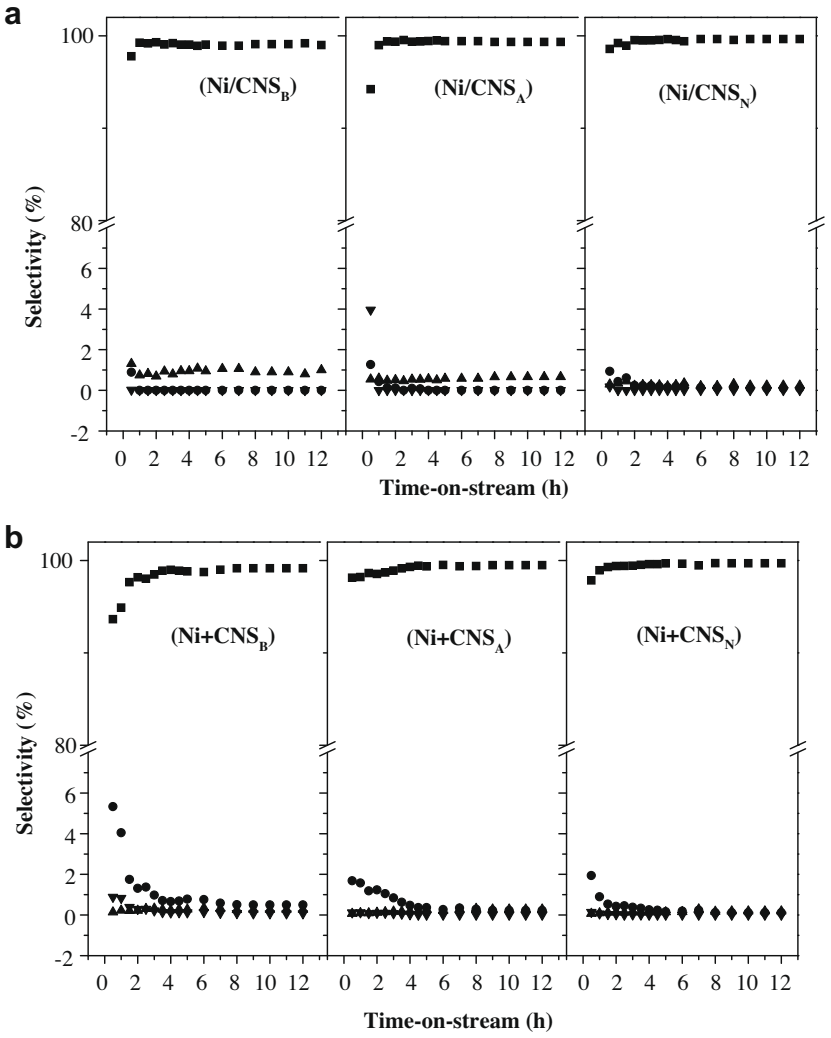


**Fig. 13.** Variation of selectivity to (■) MBA, (●) DBA, (▲) BBA and (▼) TBA with time-on-stream over (a) supported and (b) unsupported catalysts.

the range 1–5 μm (mean ≈ 2.5 μm). A detailed characterization of the bulk metal is given in a previous work [68]. Fig. 12 shows the temporal conversion associated with each physical mixture, where the following sequence of increasing activity was obtained: Ni + $CNS_B$ < Ni + $CNS_A$ < Ni + $CNS_N$. This result evidences that when the metallic phase is kept constant, the surface chemistry of carbon makes a difference on the overall catalytic activity of the system. Once again, the presence of nitrogen (preferentially in the quaternary form) plays a beneficial role in catalytic activity. In the absence of metal-support interactions or differential effects due to metal electron density, the cyano group must be further activated on $CNS_N$ than on $CNS_A$ and in turn, than on $CNS_B$. Since the adsorption of nitriles can occur both on the reduced Ni particles and on the support [64], butyronitrile must adsorb more weakly on an electron-enriched surface, favouring the catalytic activity of Ni. As commented in the experimental section, due to measurability limitations, the catalytic reactor was loaded with considerably higher amounts of metal when the unsupported catalysts were tested, what means higher contact/reaction times. Under this condition, a direct comparison between the activity delivered by supported and unsupported systems cannot be made; however, reaction rates (per unit mass of metal) were still much higher in the case of the supported catalysts (Table 3), putting in evidence the effectiveness of CNS as metal carrier.

### 3.3. Selectivity

While the role of the active metal is well recognized in the hydrogenation step, formation of higher amines is still under debate. Some authors have claimed the active metal being the most important factor determining selectivity in hydrogenation of nitriles [58,69]. Other studies, however, point to a support effect, where reactions responsible for the formation of higher amines may occur in the acid sites of the support [31,63,70,71]. Selectivity as a function of time-on-stream is shown in Fig. 13. Both the supported and the unsupported catalysts exhibited a similar temporal pattern, where selectivity to MBA was in all the cases close to 100%. A slight initial increase in selectivity to MBA (with subsequent decrease to higher amines) was concomitant with the time-on-stream deactivation observed for the six catalysts (Figs. 11 and 12) and is in good agreement with the conversion/selectivity profiles reported by Braos-García et al. [63] for the hydrogenation of acetonitrile over Ni-supported catalysts. Such a high selectivity to the primary amine must be directly linked to the surface of the supports/catalysts. As commented in the characterization section, the three CNS employed in the study delivered an essentially neutral or slightly basic character (Fig. 5), which plays against the occurrence of condensation reactions leading to higher amines. Moreover, in the range of nickel particle sizes tested (from the nano- to the micro-scale), selectivity remained practically unaffected.

## 4. Conclusions

In the present work, nickel supported on (or physically mixed with) carbon and nitrogen-doped carbon nanospheres has been successfully employed in the gas phase hydrogenation of butyronitrile, where nitrogen doping had an important impact on catalyst activity. The results generated support the following main conclusions:

(i) Nitrogen inclusion in CNS resulted in a decrease in the graphitic character of the materials and the distribution of nitrogen functionalities was dependent on the C/N source.

(ii) Upon activation, nickel delivered different particle sizes on the different supports, attributable to the electron density of the carbon surface. Nitrogen (when present), essentially in its quaternary form, led to an electron-enriched carbon surface, promoting the mobility of the metal and subsequent sintering.

(iii) Larger particles, i.e. those deposited on (essentially quaternary) nitrogen-doped surfaces, delivered higher reaction rates by weakening the adsorption strength of the C≡N group and, thus, making it easier to hydrogenate.

(iv) When nickel was physically mixed with the support, the higher electron density on the surface of the supports delivered by nitrogen inclusion also resulted in an enhanced catalytic activity.

(v) Selectivity to the primary amine was in all cases close to 100%, where the essentially neutral or slightly basic supports did not promote condensation reactions conducting to higher amines.

## Acknowledgments

The authors acknowledge financial support from Consejería de Ciencia y Tecnología de la Junta de Comunidades de Castilla-La Mancha (Project PBI-05-038 and PCI08-0020-1239). Dr. Manuel Mora (University of Córdoba) is gratefully acknowledged for assistance in XPS measurements and for stimulating discussions.

## References

[1] F. Rodríguez-Reinoso, Carbon 36 (1998) 159.
[2] D. Lozano-Castelló, M.A. Lillo-Ródenas, D. Cazorla-Amorós, A. Linares-Solano, Carbon 39 (2001) 741.
[3] F. Rodríguez-Reinoso, M. Molina-Sabio, M.T. González, Carbon 33 (1995) 15.
[4] A. Dandekar, R.T.K. Baker, M.A. Vannice, Carbon 36 (1998) 1821.
[5] A. Cuesta, P. Dhamelincourt, J. Laureyns, A. Martínez-Alonso, J.M.D. Tascón, Carbon 32 (1994) 1523.
[6] J.L. Figueiredo, M.F.R. Pereira, M.M.A. Freitas, J.J.M. Orfão, Carbon 37 (1999) 1379.
[7] C. Moreno-Castilla, M.A. Ferro-García, J.P. Joly, I. Bautista-Toledo, F. Carrasco-Martín, J. Rivera-Utrilla, Langmuir 11 (1995) 4686.
[8] S. Cahen, G. Furdin, J.F. Marêche, A. Albiniak, Carbon 46 (2008) 511.
[9] V. Gaur, R. Asthana, N. Verma, Carbon 44 (2006) 46.
[10] S. Iijima, Nature 354 (1991) 56.
[11] K.P. de Jong, J.W. Geus, Catal. Rev. – Sci. Eng. 42 (2000) 481.
[12] C. Park, M.A. Keane, J. Colloid Interface Sci. 266 (2003) 183.
[13] M.L. Toebes, F.F. Prinsloo, J.H. Bitter, A.J. van Dillen, K.P. de Jong, J. Catal. 214 (2003) 78.
[14] G.L. Bezemer, P.B. Radstake, V. Koot, A.J. van Dillen, J.W. Geus, K.P. de Jong, J. Catal. 237 (2006) 291.
[15] C. Liang, Z. Li, J. Qiu, C. Li, J. Catal. 211 (2002) 278.
[16] Z.C. Kang, Z.L. Wang, J. Mol. Catal. A: Chem. 118 (1997) 215.
[17] P. Serp, R. Feurer, Y. Kihn, P. Kalck, J.L. Faria, J.L. Figueiredo, J. Mater. Chem. 11 (2001) 1980.
[18] Y.C. Liu, X.P. Qiu, Y.Q. Huang, W.T. Zhu, Carbon 40 (2002) 2375.
[19] A. Nieto-Márquez, S. Gil, A. Romero, J.L. Valverde, S. Gómez-Quero, M.A. Keane, Appl. Catal. A: General 363 (2009) 188.
[20] O. Stephan, P.M. Ajayan, C. Colliex, Ph. Redlich, J.M. Lambert, P. Bernier, P. Lefin, Science 266 (1994) 1683.
[21] M. Glerup, M. Castignoles, M. Holzinger, G. Hug, A. Loiseau, P. Bernier, Chem. Commun. (2003) 2542.
[22] T. Maiyalagan, B. Viswanathan, Mater. Chem. Phys. 93 (2005) 291.
[23] J. Amadou, K. Chizari, M. Houllé, I. Janowska, O. Ersen, D. Bégin, C. Pham-Huu, Catal. Today 138 (2008) 62.
[24] E. Raymundo-Piñero, D. Cazorla-Amorós, A. Linares-Solano, Carbon 41 (2003) 1925.
[25] Y. Shao, J. Sui, G. Yin, Y. Gao, Appl. Catal. B: Environ. 79 (2008) 89.
[26] M.A. Keane, Appl. Catal. A: General 271 (2004) 109.
[27] C. Amorim, G. Yuan, P.M. Patterson, M.A. Keane, J. Catal. 234 (2005) 268.
[28] F. Coloma, A. Sepúlveda-Escribano, J.L.G. Fierro, F. Rodríguez-Reinoso, Appl. Catal. A: General 150 (1997) 165.
[29] S.T. McMillan, P.K. Agrawal, Ind. Eng. Chem. Res. 27 (1988) 243.
[30] M. Arai, Y. Takada, Y. Nishiyama, J. Phys. Chem. B 102 (1998) 1968.
[31] M.J.F.M. Verhaak, A.J. van Dillen, J.W. Geus, Catal. Lett. 26 (1994) 37.
[32] A. Nieto-Márquez, I. Espartero, J.C. Lazo, A. Romero, J.L. Valverde, Chem. Eng. J. 153 (2009) 211.
[33] P. Burattin, M. Che, C. Louis, J. Phys. Chem. B 101 (1997) 7060.

[34] JCPDS-ICDD, PCPDFWIN, Version 2.2, June 2001.
[35] Z.C. Kang, Z.L. Wang, J. Phys. Chem. 100 (1996) 5163.
[36] A. Nieto-Márquez, J.L. Valverde, M.A. Keane, Appl. Catal. A: General 332 (2007) 237.
[37] A. Nieto-Márquez, J.L. Valverde, M.A. Keane, Appl. Catal. A: General 352 (2009) 159.
[38] J.E. Herrera, D.E. Resasco, Chem. Phys. Lett. 376 (2003) 302.
[39] Q. Zhu, K. Grant, K.M. Thomas, Carbon 33 (1995) 35.
[40] J.M. Jones, K.M. Thomas, Carbon 33 (1995) 1129.
[41] S.D. Brown, K.M. Thomas, Fuel 72 (1993) 359.
[42] C. Park, M.A. Keane, Langmuir 17 (2001) 8386.
[43] A.G. Kudashov, A.V. Okotrub, L.G. Bulusheva, I.P. Asanov, Y.V. Shubin, N.F. Yudanov, L.I. Yudanova, V.S. Danilovich, O.G. Abrosinov, J. Phys. Chem. B. 108 (2004) 9048.
[44] V. Jiménez, P. Sánchez, J.L. Valverde, A. Romero, J. Colloid Interface Sci. 336 (2009) 712.
[45] V. Jiménez, P. Sánchez, A. de Lucas, J.L. Valverde, A. Romero, J. Colloid Interface Sci. 336 (2009) 226.
[46] J.R. Pels, F. Kapteijn, J.A. Moulijn, Q. Zhu, K.M. Thomas, Carbon 33 (1995) 1641.
[47] S. van Dommele, A. Romero-Izquirdo, R. Brydson, K.P. de Jong, J.H. Bitter, Carbon 46 (2008) 138.
[48] S. van Dommele, PhD Thesis, University of Utrecht, 2008.
[49] I. Shimoyama, G. Wu, T. Sekiguchi, Y. Baba, J. Electron. Spectrosc. 114–116 (2001) 841.
[50] M. Balón, M.C. Carmona, M.A. Muñoz, J. Hidalgo, Tetrahedron 45 (1989) 7501.
[51] M.K. van der Lee, A.J. van Dillen, J.H. Bitter, K.P. de Jong, J. Am. Chem. Soc. 127 (2005) 13573.
[52] J.H. Bitter, M.K. van der Lee, A.G.T. Slotboom, A.J. van Dillen, K.P. de Jong, Catal. Lett. 89 (2003) 139.
[53] C. Amorim, M.A. Keane, J. Chem. Technol. Biotechnol. 83 (2008) 662.
[54] A. Sepúlveda-Escribano, F. Coloma, F. Rodríguez-Reinoso, Appl. Catal. A: General 173 (1998) 247.
[55] A.E. Aksoylu, M. Madalena, A. Freitas, M.F.R. Pereira, J.L. Figueiredo, Carbon 39 (2001) 175.
[56] C.A. Bessel, K. Laubernds, N.M. Rodriguez, R.T.K. Baker, J. Phys. Chem. B 105 (2001) 1115.
[57] F. Cárdenas-Lizana, S. Gómez-Quero, M.A. Keane, Appl. Catal. A: General 334 (2008) 199.
[58] P. Braos-García, P. Maireles-Torres, E. Rodríguez-Castellón, A. Jiménez-López, J. Mol. Catal. A: Chem. 168 (2001) 279.
[59] V.V. Strelko, V.S. Kuts, P.A. Thrower, Carbon 38 (2000) 1499.
[60] S.H. Lim, H.I. Elim, X.Y. Gao, A.T.S. Wee, W. Ji, J.Y. Lee, J. Lin, Phys. Rev. B 73 (2006) 045402.
[61] V.J. Braun, G. Blessing, F. Zobel, Ber. Deutsch. Chem. Ges. B56 (1923) 1888.
[62] M.J.F.M. Verhaak, A.J. van Dillen, J.W. Geus, J. Catal. 143 (1993) 187.
[63] P. Braos-García, P. Maireles-Torres, E. Rodríguez-Castellón, A. Jiménez-López, J. Mol. Catal. A: Chem. 193 (2003) 185.
[64] F. Medina-Cabello, D. Tichit, B. Coq, A. Vaccari, N.T. Dung, J. Catal. 167 (1997) 142.
[65] A. Chojecki, M. Veprek-Heijman, T.E. Müller, P. Schärringer, S. Veprek, J.A. Lercher, J. Catal. 245 (2007) 237.
[66] C.V. Rode, M. Arai, M. Shirai, Y. Nishiyama, Appl. Catal. A: General 148 (1997) 405.
[67] H. Li, Y. Wu, Y. Wan, J. Zhang, W. Dai, M. Qiao, Catal. Today 93–95 (2004) 493.
[68] A. Nieto-Marquez, J.C. Lazo, A. Romero, J.L. Valverde, Chem. Eng. J. 144 (2008) 518.
[69] Y. Huang, W.M.H. Sachtler, Appl. Catal. A: General 182 (1999) 365.
[70] N.T. Dung, D. Tichit, B.H. Chiche, B. Coq, Appl. Catal. A: General (1998) 179.
[71] A. Infantes-Molina, J. Mérida-Robles, P. Braos-García, E. Rodríguez-Castellón, E. Finocchio, G. Busca, P. Maireles-Torres, A. Jiménez-López, J. Catal. 225 (2004) 479.